Tunnelling anisotropic magnetoresistance at $La_{0.67}Sr_{0.33}MnO_3$-graphene interfaces

L. C. Phillips[1,*], A. Lombardo[2], M. Ghidini[1,3], W. Yan[1], S. Kar-Narayan[1], S. J. Hämäläinen[4], M. Barbone[2], S. Milana[2], S. van Dijken[4], A. C. Ferrari[2] and N. D. Mathur[1,**]

[1]Department of Materials Science, University of Cambridge, Cambridge, CB3 0FS, United Kingdom.

[2]Cambridge Graphene Centre, University of Cambridge, Cambridge CB3 0FA, United Kingdom

[3]DiFeST, University of Parma, viale G.P. Usberti 7/A, 43124 Parma, Italy

[4]NanoSpin, Department of Applied Physics, Aalto University School of Science, P.O. Box 15100, FI-00076 Aalto, Finland.

[*]e-mail: lee.phillips@cantab.net

[**]e-mail: ndm12@cam.ac.uk

Using ferromagnetic $La_{0.67}Sr_{0.33}MnO_3$ electrodes bridged by single-layer graphene, we observe magnetoresistive changes of ~32-35 MΩ at 5 K. Magneto-optical Kerr effect microscopy at the same temperature reveals that the magnetoresistance arises from in-plane reorientations of electrode magnetization, evidencing tunnelling anisotropic magnetoresistance at $La_{0.67}Sr_{0.33}MnO_3$-graphene interfaces. Large resistance switching without spin transport through the non-magnetic channel could be attractive for graphene-based magnetic-sensing applications.

Graphene is a candidate material for spintronics[1,2] because its low spin-orbit coupling has prompted predictions[3,4] of long spin-diffusion length l_{sf}. This is a prerequisite for spin logic proposals[5,6], but many non-local (four-terminal) studies of spin transport and precession report moderate values of l_{sf} of order 1 μm[7-12], with the largest l_{sf} ~ 24 μm for graphene encapsulated by hexagonal boron nitride [13]. For multilayer graphene grown on the C-face of SiC, a much greater value of $l_{sf} \sim 200$ μm was inferred[14] from large field-driven changes of local (i.e. two-terminal) resistance $\Delta R \sim 1.5$ MΩ, but these changes were quasi-continuous and therefore inconsistent with the assumption of parallel/antiparallel electrode magnetizations.

Interpreting local magnetoresistance (MR) is difficult because it can arise from non-spin-transport effects that include anisotropic magnetoresistance (AMR)[15,16] and magnetic domain-wall resistance[17-19] in the electrodes, the local Hall effect[20], the magneto-Coulomb effect[21] and tunnelling anisotropic magnetoresistance (TAMR)[22-26].

TAMR[22-26] arises when there is tunnelling across a resistive tunnel barrier, on one side of which lies a ferromagnetic electrode that undergoes non-180° magnetic switching. This happens because spin-orbit coupling in the ferromagnet couples magnetization direction to the tunnelling density of states[22], such that TAMR adopts the symmetry of the electrode if the tunnel barrier is centrosymmetric[24]. For example, TAMR ~ 3% was recorded[25] at 4.2 K for an interface between an organic semiconductor and highly spin-polarised[27,28] $La_{0.67}Sr_{0.33}MnO_3$ (LSMO) electrodes.

Here we report the first observation of TAMR at interfaces that form spontaneously between LSMO and graphene, specifically single-layer graphene (SLG). Two-terminal measurements at 5 K indicate high resistance (hundreds of MΩ) and TAMR ≤ 7%. Magneto-optical Kerr effect (MOKE) data show that our LSMO electrodes undergo 90° magnetic switching at the magnetotransport measurement temperature in all devices that show MR, which is thus identified as TAMR. The absolute change of resistance $\Delta R \sim 35$ MΩ is much greater than the value reported in Ref. 25, and would imply a very large $l_{sf} \sim 1$ mm if interpreted as spin transport, as previously done in Ref. 14.

Our devices are fabricated following the scheme in Fig. 1(a), with an SLG channel connecting LSMO electrodes patterned from epitaxial films grown on the (001)

surface of orthorhombic $NdGaO_3$ (NGO). In principle one could try and align the single magnetic easy axis[29] parallel to $[010]_{NGO}$ across the width of each electrode, in order to achieve coercivity contrast via magnetic shape anisotropy using electrodes of different width. In this case, parallel and antiparallel magnetic configurations could arise in adjacent electrodes while sweeping the magnetic field, such that any measured MR would be due to spin transport[30]. However, this type of magnetic switching may not occur for two reasons. First, off-stoichiometry or partial relaxation can produce magnetically biaxial behaviour[31] below ~200 K. Second, NGO can form twins (on $\{110\}_{NGO}$ and $\{112\}_{NGO}$ planes)[32] that modify the local magnetic anisotropy of epitaxial films grown on top. Here we achieve TAMR via each of these two scenarios in two devices fabricated on separate substrates, and we use MOKE to verify magnetic switching at the 5 K measurement temperature. We also find further evidence for TAMR in a third device using a magnetic field applied out-of-plane (OOP) rather than in-plane.

Epitaxial LSMO films ~40 nm thick are grown on NGO (001) by pulsed laser deposition as for Ref. 33, and characterized using atomic force microscopy (AFM) and x-ray diffraction (XRD). Electrodes (length ~30 μm, width 2-10 μm, separation 1-3 μm) and wirebond pads (400 μm × 350 μm) are then defined in LSMO by photolithography and Ar-ion milling, using different processing routes for our three devices. For Device 3, a 5 nm-thick protective layer of Au is evaporated before electrode definition and removed in an aqueous solution of KI/I_2 after electrode definition. The space between electrodes is backfilled with amorphous SiO_2 to minimise electrode side contact with SLG (Supplementary Note 1). Device 2 is processed with the Au step alone. Device 1 is processed with neither step.

Graphene is produced onto oxidised Si wafers by micromechanical cleavage of natural graphite (NGS Naturgrafit)[34] and identified by a combination of optical contrast[35] and Raman spectroscopy[36,37]. Raman spectroscopy is also used to ensure high structural quality and evaluate chemical doping. The flakes are subsequently transferred onto pre-patterned electrodes by a wet transfer process[38,39]. A polymethyl methacrylate (PMMA) scaffold is spun on the flakes, and detached from the substrate by soaking in de-ionized (DI) water. The water intercalates at the interface between the hydrophilic SiO_2 and the hydrophobic PMMA, gently releasing the PMMA film. SLG flakes remain attached to

the bottom of the freestanding PMMA film, subsequently placed onto the LSMO electrodes in DI water (Device 1) or a mixture of isopropanol and DI water (Devices 2 and 3). After removing the water, the PMMA layer is dissolved with acetone, releasing the flakes onto the LSMO electrodes. Raman measurements are performed using a Renishaw InVia micro-spectrometer equipped with a ×100 objective (numerical aperture, N.A. = 0.85), a laser excitation wavelength of 514.5 nm before transfer, and 457, 488, 514.5 nm after transfer, with an incident laser power below 500 μW to avoid local heating or damage.

For dc magnetotransport measurements, we contact LSMO wirebond pads via Al wirebonds and In pads, and use a Janis cryostat and a Keithley picoammeter with built-in voltage source. The magnetic field *H* applied parallel to the electrode short axes is varied quasistatically. A current could not be passed between all electrodes, which rules out parasitic conduction pathways, but renders four-terminal measurements impossible. Therefore we present two-terminal measurements of resistance. MOKE measurements are then performed at 5 K using an imaging system from Evico Magnetics with a continuous-flow He cryostat (Janis ST-500). The measurements are conducted in longitudinal Kerr geometry[40] (in-plane magnetic field parallel to the plane of incident light). Given the small size of our electrodes, magnetic hysteresis curves (with an in-plane magnetic field applied parallel and perpendicular to electrode long axes) are obtained by restricting the data collection to LSMO contact areas, with In pads and wirebonds removed. Linear Faraday contributions from the cryostat cover glass and the microscope objectives are also removed after data collection.

XRD (Supplementary Note 2) confirms that our LSMO films are epitaxial and highly strained with respect to the substrate, whose orthorhombic distortion they therefore inherit. XRD reveals twinning on $\{110\}_{NGO}$ but not $\{112\}_{NGO}$ planes. AFM confirms that as-grown LSMO films are flat away from unit-cell-high vicinal steps [Fig. 1(b)]. After milling to define electrodes in Devices 2 and 3, removing the protective layer of Au exposes a surface with residual contamination (see AFM phase signal), but the original stepped surface is restored after wiping with cotton buds soaked in isopropanol. Following transfer, graphene is optically invisible [Fig. 1(c)], but can be still probed with AFM (Supplementary Note 3) and Raman spectroscopy [Fig. 1(d,e)].

Complete optical microscopy images for Devices 2 and 3 are available in Supplementary Note 4.

We investigate the structural quality and doping of graphene before and after transfer by Raman spectroscopy. The 514.5 nm Raman spectrum of exfoliated graphene on SiO_2 before transfer [Fig. 1(d), black curve] contains a single Lorentzian 2D peak[36] with full-width-at-half-maximum FWHM ~ 26 cm^{-1}, which confirms that the sample is SLG. The absence of a prominent D peak at ~1350 cm^{-1} indicates negligible defects. From the G-peak position [Pos(G) ~ 1582 cm^{-1}] and FWHM [FWHM(G) ~ 13 cm^{-1}], the 2D-G peak intensity [I(2D)/I(G) ~ 3.7] and area [A(2D)/A(G) ~ 8.2] ratios, we derive a doping level <200 meV[41,42]. After transfer, a background signal [Fig. 1(d), blue curve] from Nd^{3+} photoluminescence[43,44] overshadows the G and 2D peaks [Fig. 1(d), red curve], but is displaced when the excitation wavelength is changed to 488 nm [Fig. 1(e)]. A point-to-point subtraction of spectra of LSMO/NGO regions, with [Fig. 1(e), black curve] and without [Fig. 1(e), blue curve] transferred graphene, and normalized to the NGO Raman peak at ~470 cm^{-1}, yields a clear graphene Raman spectrum [Fig. 1(e), red curve]. Here the single Lorentzian 2D peak, with FWHM ~ 28 cm^{-1} and absence of a prominent D peak, imply negligible defects. From Pos(G) ~ 1583 cm^{-1}, FWHM(G) ~14 cm^{-1}, I(2D)/I(G) ~ 5.2 , A(2D)/A(G) ~ 3, we estimate a doping ~100 meV[41,42], corresponding to a carrier density $n \sim 10^{12}$ cm^{-2}.

At low temperatures, the resistance R between conducting electrode pairs (Devices 1 and 2) is unaffected by SiO_2 backfilling (Device 3), suggesting that conduction occurs primarily via the LSMO film surface, and not through milled LSMO sidewalls. At bias below ~100 mV, we find 100 MΩ < R < 1 GΩ, whereas non-linearity at higher bias [Fig. 1(f)] indicates that LSMO-graphene interfaces function as tunnel barriers, cf. spin-valves based on LSMO electrodes and carbon nanotubes[45]. A Brinkman fit[46] using our measured interfacial areas would require a 4 nm barrier to form spontaneously. For direct contact between an LSMO surface and much thinner SLG, this would be plausible only in the presence of a substantial surface layer of suppressed conductivity in LSMO (the so-called ‘dead’ layer). We neglect this possibility here because the LSMO surface magnetism is only partially suppressed[47] at low temperatures,

i.e. the 'dead' layer retains some magnetic order. Instead, we infer from the fit that the LSMO-SLG contact is inhomogeneous.

Devices 1 and 2 show a distinctive MR signal at 5 K [Fig. 2(a,b)]. For Device 1, we observe two peaks in MR, as seen for spin transport[7, 14, 28,45], with $\Delta R \sim 35$ MΩ and $MR \sim 3\%$ [$MR = \Delta R/R_{min}$], where $R_{min} = 858.4$ MΩ is the lowest resistance observed at $\mu_0 H = -78$ mT. For Device 2, we observe two peaks that overlap at $H = 0$, with $\Delta R \sim 32$ MΩ and $MR \sim 7\%$, where $R_{min} = 461.7$ MΩ at $\mu_0 H = -43$ mT. On increasing temperature to 20 K, we see a rapid fall of MR to ~1% (Supplementary Note 6).

The electrical switching in Device 1 occurs at fields ($|\mu_0 H| \sim 50$ mT and 100 mT) that exceed the $|\mu_0 H| \sim 10$ mT switching field measured biaxially in a nearby wirebond pad [Fig. 2(c)]. This biaxial behaviour is occasionally observed in LSMO at low temperatures due to off-stoichiometry or partial relaxation[31]. Assuming the switching fields of the electrodes to be larger than those for the wirebond pads, due to larger demagnetising fields, we identify the 50 mT switching with the wider electrode C, and the 100 mT switching with the narrower electrode D. The switching in Device 2 is associated with uniaxial magnetic switching in a nearby wirebond pad, but the easy axis lay parallel to electrode lengths not widths [Fig. 2(d)]. This suggests that Device 2 sits on a twin in which $[100]_{NGO}$ and $[010]_{NGO}$ are exchanged (Supplementary Note 2).

In order to establish that the observed peaks in $R(H)$ arise from TAMR, we first rule out several other possible causes based on MR magnitude alone. Intrinsic MR in the LSMO electrodes and SLG cannot be responsible, as our values of ΔR are 10^5 times larger than the resistance of either material (since an LSMO electrode with resistivity 10^{-4} Ω cm, length $L = 30$ μm, width $W = 3$ μm and thickness 40 nm has resistance 250 Ω; and a SLG channel region with sheet resistance 1 kΩ square^{-1}, $L = 3$ μm and $W = 30$ μm has resistance 100 Ω). Domain walls in the LSMO electrodes cannot be responsible, as even a dense array in our narrowest electrode D would only change R by tens of kΩ at most (an array of 180° domain walls with resistance-area product[18] 1.4×10^{-11} Ω cm^2, spaced every 100 nm in a 30 μm-long electrode of thickness 40 nm and width 1.5 μm yields $\Delta R \sim 70$ kΩ). Local Hall voltages in SLG cannot be responsible, as they are limited to the kΩ range by the Hall coefficient of graphene and LSMO fringing fields (an SLG flake with carrier density $n = 10^{12}$ cm^{-2}, consistent with the Raman estimates, has Hall

coefficient $R_H = 1/(ne) \approx 600\ \Omega\ T^{-1}$, the fringing flux density at the LSMO sidewall is $B \sim 1$ T, and so a flake carrying current $I = 1$ nA would develop transverse Hall voltage $|V_H| = IBR_H \sim 600$ nV). Magneto-Coulomb effects cannot be responsible, as they occur only in the Coulomb blockade regime, at temperatures and biases 3-4 orders of magnitude too small (an SLG/LSMO interface with relative permittivity $\varepsilon_r = 1$, area $A = 900\ \mu m^2$ and thickness $d = 1$ nm has capacitance $C = \varepsilon_r \varepsilon_0 A/d \sim 0.8$ pF, such that Coulomb blockade would require $V < e/2C \sim 100$ nV and $T < (e^2/2C)/k_B \sim 1$ mK).

We also rule out spin transport in view of the MR magnitude, using the formalism developed in Refs. 48 and 49. To do so, we calculate ΔR for parallel and antiparallel electrode configurations in a two-terminal device with a single spin-dependent resistance $R_{+(-)} = 2R_b(1-(+)\gamma)$ at each LSMO-SLG interface, where + (-) signifies majority (minority) spin electrons with respect to LSMO magnetization, and γ is the interfacial spin polarisation. In our highly resistive devices, R_b greatly exceeds both the ferromagnet spin resistance $R_F = \rho_F l_{sf}^F / (1-\beta^2) A_F$ and the channel spin resistance $R_{ch}^s = R_{sq} l_{sf} / w$, where ρ_F, l_{sf}^F and β are resistivity, spin diffusion length and current spin polarisation in the ferromagnet, R_{sq} is the SLG sheet resistance, and the channel has width w and length L. In this regime, ΔR has a strict upper bound[14], $\Delta R \le 4\gamma^2 R_{ch}^s l_{sf} / L$. This gives a lower bound for l_{sf} as follows. Taking $\gamma = 0.8$ [Ref. 45], $R_{sq} = 1\ k\Omega$ square^{-1} and $w = 30\ \mu m$, we find that the observed values of ΔR would require $l_{sf} = 0.64$ mm in Device 1 ($L = 1\ \mu m$), and $l_{sf} = 1.06$ mm in Device 2 ($L = 3\ \mu m$). These millimetre-scale spin diffusion lengths are 1-2 orders of magnitude longer than predictions for intrinsic SLG[3,4], and 1-3 orders of magnitude above existing experimental values[7-13, 50]. Moreover, l_{sf} would be even larger if we took into account the unequal electrode areas, and the possibility of imperfect switching[30]. Therefore unrealistically large improvements in l_{sf} would be required to explain the magnitude of our MR peaks in terms of spin transport.

Combining the above process of elimination with our MOKE data, we infer that the observed peaks in $R(H)$ arise from TAMR. In our orthorhombic films of LSMO, 90° rotations of magnetization permit TAMR, whereas 180° rotations would permit no TAMR. For Device 1, 90° rotations can arise due to the biaxial magnetic anisotropy [31], consistent with Fig. 2(c). For Device 2 on an NGO twin, electrode magnetization lies

lengthwise at remanence and rotates 90° for $|\mu_0 H| > 20$ mT [Fig. 2(d)]. The form of the observed MR in each device [Fig. 2(a,b)] is therefore consistent with TAMR, and so we rule out spin transport. We note that TAMR could even be generated by LSMO electrodes with uniaxial aisotropy, if they switch via a dense array of domain walls[30] in which the magnetization is locally oblique.

The TAMR magnitude in our devices is similar to the low-temperature values obtained with LSMO electrodes[25,26]. However, TAMR in Device 1 is reduced with respect to Device 2, probably because structural relaxation reduces the degree of LSMO distortion (Supplementary Note 2). More generally, the interpretation of bias-dependent TAMR is challenging[24, 51], as it is influenced by all of the electronic bulk/interfacial states in the electrodes[51]. This complexity is rich enough to explain why Devices 1 and 2 differ in terms of which electrode magnetization direction corresponds to the low-resistance state [Fig. 2].

MR measurements with an out-of-plane (OOP) magnetic field yield $R(H)$ data that are more symmetric and anhysteretic [Device 3, Fig. 3] than the corresponding data obtained with an in-plane field [Fig. 2(a,b)]. There is a decrease in R on increasing applied field magnitude to $|\mu_0 H| \approx 100$ mT, followed by an increase prior to reaching our maximum measurement field. We suggest that this MR also arises due to TAMR associated with electrode magnetization canting to develop an OOP component. This can result in $R(H)$ extrema[23], and our minima correspond to canting angles of around $\pm 30°$. We note that Fig. 3 superficially resembles the Hanle curve expected from spin transport, but given that we rule out spin transport as explained above, fitting to a Hanle expression (as in the Supplementary Information of Ref. 52) would yield meaningless parameters.

In summary, we studied LSMO/SLG interfaces in lateral devices, and observed MR ranging from ~3-7% and ΔR from ~32-35 MΩ. These changes appear too large to be explained by spin transport in SLG. Instead, we attribute them to TAMR at the interface between SLG and orthorhombic LSMO, consistent with the 90° magnetic domain switching evidenced by MOKE. MR data obtained with an out-of-plane magnetic field are also attributed to TAMR arising from a canted electrode magnetization, as it is coincidental that the spin relaxation time is consistent with spin transport. Our work

highlights the need to verify electrode switching in spintronic devices, and presents a large MR in SLG that may be exploited for magnetic field sensing.

Acknowledgements

We thank V. Garcia, M. Bibes, P. Seneor and A. Fert for useful discussions. This work was funded by grant F/09 154/E from the Leverhulme Trust, ERC Grant Hetero2D, EU Graphene Flagship (no. 604391), a Schlumberger Cambridge International Scholarship, a UK EPSRC DTA award, the Royal Society, and EPSRC Grants EP/K01711X/1, EP/K017144/1, EP/N010345/1, EP/M507799/1 and EP/L016087/1.

References

1. P. Seneor, B. Dlubak, M.-B. Martin, A. Anane, H. Jaffres and A. Fert, *MRS Bulletin* **37**, 1245 (2012).

2. A. C. Ferrari *et al.*, *Nanoscale* **7,** 4598 (2015).

3. D. Huertas-Hernando, F. Guinea and A. Brataas, *Phys. Rev. Lett.* **103**, 146801 (2009).

4. D. Pesin and A. H. MacDonald, *Nature Materials* **11**, 409 (2012).

5. H. Dery, L. Cywinski, P. Dalal and L. Sham, *Nature* **447**, 573 (2007).

6. B. Behin-Aein, D. Datta, S. Salahuddin and S. Datta, *Nature Nanotechnology* **5**, 266 (2010).

7. N. Tombros, C. Jozsa, M. Popinciuc, H. T. Jonkman and B. J. van Wees, *Nature* **448**, 571 (2007).

8. W. Han, K. Pi, W. Bao, K. M. McCreary, Y. Li, W. H. Wang, C. N. Lau and R. K. Kawakami, *Appl. Phys. Lett.* **94**, 222109 (2009).

9. W. Han and R. K. Kawakami, *Phys. Rev. Lett.* **107**, 047207 (2011).

10. T. Maassen, J. J. Van den Berg, N. Ijbema, F. Fromm, T. Seyller, R. Yakimova and B. J. van Wees, *Nano Lett.* **12**, 1498 (2012).

11. M. H. D. Guimarães, A. Veligura, P. J. Zomer, T. Maassen, I. J. Vera-Marun, N. Tombros and B. J. van Wees, *Nano Lett.* **12**, 3512 (2012).

12. P. J. Zomer, M. H. D. Guimarães, N. Tombros and B. J. van Wees, *Phys. Rev. B* **86**, 161416 (2012).

13. J. Ingla-Aynés, M. H. D. Guimarães, R. J. Meijerink, P. J. Zomer and B. J. van Wees, *Phys. Rev. B* **92**, 201410(R) (2015).

14. B. Dlubak, M.-B. Martin, C. Deranlot, B. Servet, S. Xavier, R. Mattana, M. Sprinkle, C. Berger, W. A. de Heer, F. Petroff, A. Anane, P. Seneor and A. Fert, *Nature Physics* **8**, 557 (2012).

15. T. R. McGuire and R. L. Potter, *IEEE Trans. Mag.* **11**, 1018 (1975).

16. J.-B. Yau, X. Hong, A. Posadas, C. H. Ahn, W. Gao, E. Altman, Y. Bason, L. Klein, M. Sidorov and Z. Krivokapic, *J. Appl. Phys.* **102**, 103901 (2007).

17. N. D. Mathur, P. B. Littlewood, N. K. Todd, S. P. Isaac, B.-S. Teo, D.-J. Kang, E. J. Tarte, Z. H. Barber, J. E. Evetts and M. G. Blamire, *J. Appl. Phys.* **86,** 6287 (1999).

18. J. Wolfman, A. M. Haghiri-Gosnet, B. Raveau, C. Vieu, E. Cambril, A. Cornette and H. Launois, *J. Appl. Phys.* **89**, 6955 (2001).

19. L. Granja, L. E. Hueso, P. Levy and N. D. Mathur, *Appl. Phys. Lett.* **103**, 062404 (2013).

20. P. K. Muduli, J. Barzola-Quiquia, S. Dusari, A. Ballestar, F. Bern, W. Böhlmann and P. Esquinazi, *Nanotechnology* **24**, 015703 (2013).

21. S. J. van der Molen, N. Tombros and B. J. van Wees, *Phys. Rev.B* **73**, 220406 (2006).

22. C. Gould, C. Rüster, T. Jungwirth, E. Girgis, G. M. Schott, R. Giraud, K. Brunner, G. Schmidt and L. W. Molenkamp, *Phys. Rev. Lett.* **93**, 117203 (2004).

23. C. Rüster, C. Gould, T. Jungwirth, J. Sinova, G. M. Schott, R. Giraud, K. Brunner, G. Schmidt and L. W. Molenkamp, *Phys. Rev. Lett.* **94**, 027203 (2005).

24. J. Moser, A. Matos-Abiague, D. Schuh, W. Wegscheider, J. Fabian and D. Weiss, *Phys. Rev. Lett.* **99**, 056601 (2007).

25. M. Grünewald, M. Wahler, F. Schumann, M. Michelfeit, C. Gould, R. Schmidt, F. Würthner, G. Schmidt and L. W. Molenkamp, *Phys. Rev. B* **84**, 125208 (2011).

26. M. Grünewald, N. Homonnay, J. Kleinlein and G. Schmidt, *Phys. Rev. B* **90**, 205208 (2014).

27. J.-H. Park, E. Vescovo, H.-J. Kim, C. Kwon, R. Ramesh and T. Vankatesan, *Nature* **392,** 794-796 (1998).

28. M. Bowen, M. Bibes, A. Barthélémy, J.-P. Contour, A. Anane, Y. Lemaître and A. Fert, *Appl. Phys. Lett.* **82**, 233 (2003).

29. H. Boschker, M. Mathews, E. P. Houwman, H. Nishikawa, A. Vailionis, G. Koster, G. Rjinders and D. H. A. Blank, *Phys. Rev. B* **79**, 214425 (2009).

30. L. C. Phillips, W. Yan, X. Moya, M. Ghidini, F. Maccherozzi, S. S. Dhesi and N. D. Mathur, *Phys. Rev. Applied* **4**, 064004 (2015).

31. L. C. Phillips, M. Ghidini, X. Moya, F. Maccherozzi, S. S. Dhesi and N. D. Mathur, *J. Phys. D: Appl. Phys.* **46**, 032002 (2013).

32. R. Uecker, P. Reiche, V. Alex, J. Doerschel and R. Schalge, *J. Cryst. Growth* **137**, 278 (1994).

33. L. C. Phillips, F. Maccherozzi, X. Moya, M. Ghidini, W. Yan, J. Soussi, S. S. Dhesi and N. D. Mathur, *J. Magn. Magn. Mater.* **355**, 331 (2014).

34. K. Novoselov, D. Jiang, F. Schedin, T. J. Booth, V. V. Khotkevich, S. V. Morozov and A. K. Geim, *Proc. Natl. Acad. Sci.* **102**, 10451 (2005).

35. C. Casiraghi, A. Hartschuh, E. Lidorikis, H. Qian, H. Harutyunyan, T. Gokus, K. S. Novoselov and A. C. Ferrari, *Nano Letters* **7**, 2711 (2007).

36. A. C. Ferrari, J. C. Meyer, V. Scardaci, C. Casiraghi, M. Lazzeri, F. Mauri, S. Piscanec, D. Jiang, K. S. Novoselov, S. Roth and A. K. Geim, *Phys. Rev. Lett.* **97**, 187401 (2006).

37. A. C. Ferrari, D. M. Basko, *Nature Nanotechnology* **8**, 235 (2013).

38. A. Reina, H. Son, L. Jiao, B. Fan, M. S. Dresselhaus, Z. Liu and J. Kong, *J. Phys. Chem. C* **112**, 17741 (2008).

39. F. Bonaccorso, A. Lombardo, T. Hasan, Z. Sun, L. Colombo, A. C. Ferrari, *Materials Today* **15**, 564 (2012).

40. M. Freiser, *IEEE Trans. Mag.* **4**, 152 (1968).

41. A. Das, S. Pisana, B. Chakraborty, S. Piscanec, S. K. Saha, U. V. Waghmare, K. S. Novoselov, H. R. Krishnamurthy, A. K. Geim, A. C. Ferrari, A. K. Sood, *Nature Nanotechnology*, **3**, 210 (2008).

42. D. M. Basko, S. Piscanec and A. C. Ferrari, *Phys. Rev. B* **80**, 165413 (2009).

43. X. Zhang, C. Serrano, E. Daran, F. Lahoz, G. Lacoste, and A. Muñoz-Yagüe *Phys. Rev. B* **62**, 4446 (2000).

44. A. Mendioroz, R. Balda, M. Voda, M. Al-Saleh and J. Fernández, *Optical Materials* **26**, 351 (2004).

45. L. E. Hueso, J. M. Pruneda, V. Ferrari, G. Burnell, J. P. Valdés-Herrera, B. D. Simons, P. B. Littlewood, E. Artacho, A. Fert and N. D. Mathur, *Nature* **445**, 410 (2007).

46. W. F. Brinkman, R. C. Dynes and J. M. Rowell, *J. Appl. Phys.* **41**, 1915 (1970).

47. M. J. Calderón, L. Brey and F. Guinea, *Phys. Rev. B* **60**, 6698 (1999).

48. T. Valet and A. Fert, *Phys. Rev. B* **48**, 7099 (1993).

49. A. Fert and H. Jaffrès, *Phys. Rev. B* **64**, 184420 (2001).

50. W. Yan, L. C. Phillips, M. Barbone, S. Hämäläinen, A. Lombardo, M. Ghidini, X. Moya,, F. Maccherozzi, S. van Dijken, S. S. Dhesi, A. C. Ferrari and N. D. Mathur, manuscript in preparation.

51. A. N. Chantis, K. D. Belaschenko, E. Y. Tsymbal and M. van Schilfgaarde, *Phys. Rev. Lett.* **98**, 046601 (2007).

52. Y. Fukuma, L. Wang, H. Idzuchi, S. Takahasi, S. Maekawa and Y. Otani, *Nature Materials* **10**, 527 (2011).

Figure 1

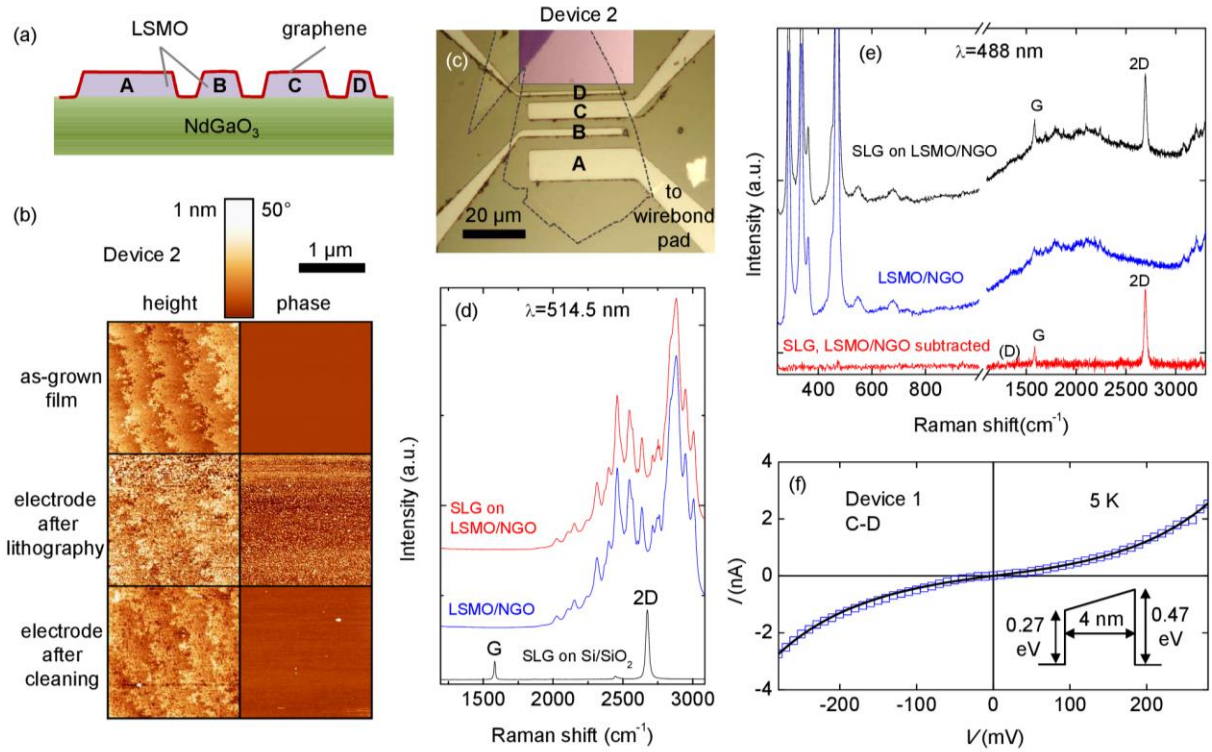

Figure 1. Graphene and LSMO electrodes. (a) Device schematic showing LSMO electrodes A-D, conformally coated with SLG (red). [Electrode widths are A (10 μm), B (3 μm), C (6 μm) and D (2 μm). Electrode spacings are A-B (3 μm), B-C (2 μm) and C-D (1 μm).] (b) AFM images of an electrode in Device 2 at different stages of processing. (c) Composite optical microscopy image, showing SLG on SiO_2 before transfer (central inset at top), and graphene on LSMO electrodes in Device 2 after transfer (main image). Dashed line denotes SLG border identified by overlaying the inset image, a procedure validated by AFM in other samples. Multilayer region (dark in top left of inset) does not bridge electrodes. (d) Raman spectra of graphene on SiO_2 before transfer, and on LSMO/NGO after transfer. (e) Raman spectra of graphene on LSMO/NGO after transfer showing background correction. (f) Current (I) versus voltage (V) for electrodes C and D of Device 1 at 5 K (open symbols), and from a Brinkman fit for back-to-back asymmetric tunnel barriers (black line). Inset: fitted barrier shape.

Figure 2

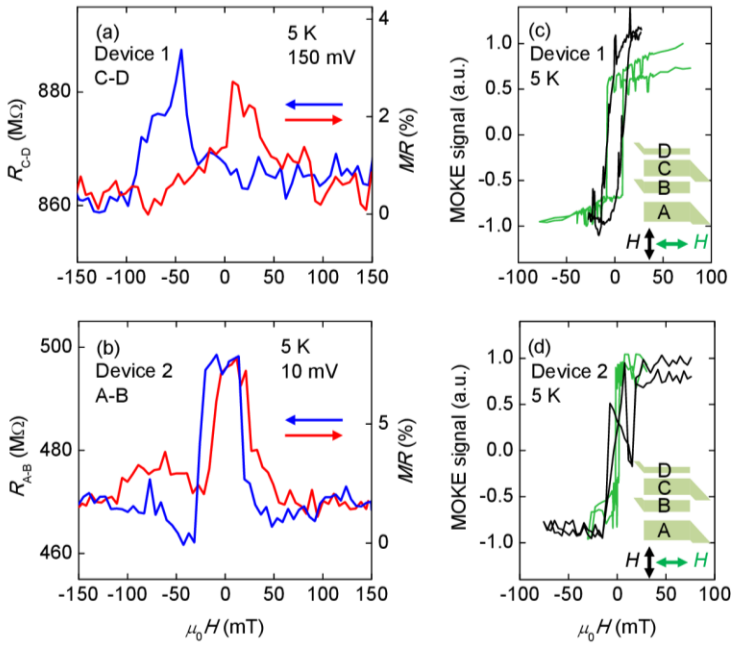

Figure 2. Magnetoresistance and MOKE at 5 K. Resistance $R(H)$ and magnetoresistance $MR(H) = \Delta R(H)/R_{min}$ measured between (a) electrodes C-D (Device 1, bias 150 mV) and (b) A-B (Device 2, bias 10 mV), with magnetic field H applied along electrode widths. (c,d) MOKE signal from nearby wirebond pad, with H applied along electrode widths (black data) and lengths (green data). Hard-axis data in (d) show an unexpected discontinuity. Resistance data are averaged over 3 [Device 1] and 10 [Device 2] sweeps of magnetic field. Raw data appear in Supplementary Note 5.

Figure 3

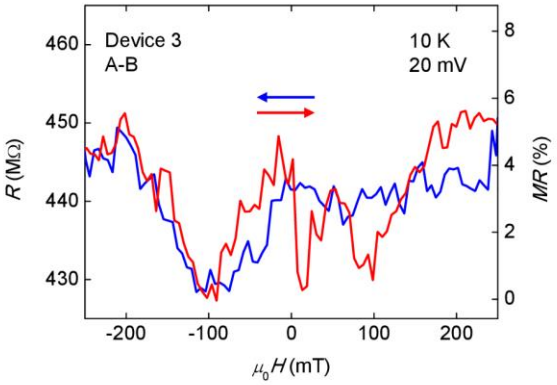

Figure 3. Magnetoresistance at 10 K with out-of-plane applied field. Resistance $R(H)$ and magnetoresistance $MR(H) = \Delta R(H)/R_{min}$ measured between electrodes A-B (Device 3, bias 20 mV), with magnetic field H applied out of the LSMO film plane. Resistance data are averaged over 10 sweeps of magnetic field. Raw data appear in Supplementary Note 5.